PROGRESS IN PHOTOVOLTAICS: RESEARCH AND APPLICATIONS
Prog. Photovolt: Res. Appl. (2010)
Published online in Wiley Online Library (wileyonlinelibrary.com). DOI: 10.1002/pip.1062

APPLICATIONS

Impurity-to-efficiency simulator: predictive simulation of silicon solar cell performance based on iron content and distribution

J. Hofstetter[1]*, D. P. Fenning[2], M. I. Bertoni[2], J. F. Lelièvre[3], C. del Cañizo[1] and T. Buonassisi[2]

[1] Instituto de Energía Solar, Universidad Politécnica de Madrid, 28040 Madrid, Spain
[2] Massachusetts Institute of Technology, Cambridge, MA 02139, USA
[3] Centro de Tecnología del Silicio Solar *CENTESIL*, Madrid, Spain

ABSTRACT

We present a simulation tool that predicts solar cell efficiency based on iron content in as-grown wafer and solar cell processing conditions. This "impurity-to-efficiency" (I2E) simulation tool consists of three serial components, which are independently and jointly validated using published experimental results: (1) a kinetic model that calculates changes in the distribution of iron and phosphorus atoms during annealing; (2) an electronic model that predicts depth-dependent minority carrier lifetime based on iron distribution; and (3) a device simulator that predicts solar cell performance based on the minority carrier lifetime distribution throughout the wafer and the device architecture. The I2E model is demonstrated to be an effective predictor of cell performance for both single-crystalline and multi-crystalline silicon solar cells. We demonstrate the process optimization potential for the I2E simulator by analyzing efficiency improvements obtained using low-temperature annealing, a processing concept that has been successfully applied to achieve higher solar cell efficiencies on Fe-contaminated materials. Copyright © 2010 John Wiley & Sons, Ltd.

KEYWORDS
silicon solar cells; simulation; gettering; impurities

***Correspondence**
J. Hofstetter, Instituto de Energía Solar, Universidad Politécnica de Madrid, 28040 Madrid, Spain.
E-mail: jasmin.hofstetter@ies-def.upm.es

Received 17 May 2010; Revised 23 August 2010

1. INTRODUCTION

Silicon solar cell performance depends strongly on how well the cell fabrication process is matched to the quality of the wafer source material. Because of the non-linear effects of cell processing on the electronic properties of the material, the final charge carrier lifetime measured on a solar cell cannot be easily deduced from the initial lifetime measured on the as-grown wafer [1]. Therefore, given the breadth of material quality in the crystalline silicon market—from high purity, single crystal (sc-Si) grown by the Czochralski technique to directionally-solidified upgraded metallurgical grade multi-crystalline (mc-Si) wafers—one might expect an equally varied set of manufacturing conditions. However, such source-specific tailoring of cell processing is limited by the high-dimensional parameter space of cell processing and the resulting monetary and temporal cost associated with conducting a design of experiment to find local or global efficiency maxima.

In particular, the time–temperature profiles in a standard solar cell process have been developed for electronic grade Si (EG-Si) but are not well-adapted for solar grade Si (SoG-Si) because of the much higher impurity concentrations in SoG-Si. Tentative specifications of the acceptable impurity levels in SoG-Si given standard cell processing can be found in Reference [2,3]. In EG-Si, the low total concentration of impurity atoms facilitates the complete dissolution of precipitates and the removal of fast-diffusing species, i.e., Fe, Cr, Ni, and Cu, which is accomplished by means of external gettering during phosphorus emitter diffusion. In contrast, because of the high contamination levels in SoG-Si, high-temperature steps have been predicted to lead to only the partial dissolution of metal precipitates during the short phosphorous diffusion gettering (PDG) applied in a typical industrial solar cell process [4,5]. To extract the full efficiency potential from low-quality wafers, the industrial process needs to be adapted to accommodate SoG-Si, as well as to enhance performance of cells originating from

Copyright © 2010 John Wiley & Sons, Ltd.

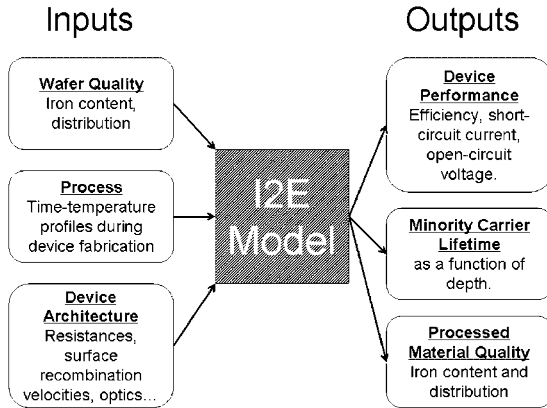

Figure 1. Required inputs and resulting outputs of the I2E simulator.

areas of the ingot that contain higher impurity contents (e.g., edge, top, and bottom regions). In these "red zone" areas, iron is usually the dominant impurity [6,7]. Thus far, the flexible adaptation of the solar cell fabrication process to each source material has been a resource-intensive task due to the lack of predictive capability.

In this manuscript, we present a simulation tool that predicts final solar cell performance given inputs of material quality, cell processing conditions, and cell architecture, as shown in Figure 1. This "Impurity-to-Efficiency" (I2E) simulator assumes that iron is the dominant lifetime-limiting impurity, an approximation that is accurate in many regions of a standard mc-Si ingot.

Besides its predictive capability, the integrated I2E model allows one to design a solar cell process adapted to measurable material properties, i.e., total iron concentration and distribution. The model can serve as a guide to researchers and manufacturers working toward optimizing processing parameters, saving time and money.

2. MODEL DESCRIPTION

Our I2E simulator, as shown in Figure 1, calculates the impact of impurity content and distribution on final cell efficiency as a function of thermal processing. It consists of three standalone modeling blocks: (A) a diffusion-gettering simulator that models the evolution of iron distribution during cell processing, (B) a Shockley-Read-Hall-based lifetime model for converting as-processed Fe_i impurity distribution to effective minority carrier lifetime, and (C) the *PC1D* open-source device simulation software [8]. A description and independent validation of each modeling block follows below.

2.1. Iron redistribution during solar cell processing

Our model describes the evolution of the dissolved and precipitated iron distribution during the solar cell fabrication process, taking into account segregation of iron to a diffused phosphorus layer and the dissolution of iron from iron silicide precipitates. The dissolved iron concentration, $C_i(x, t)$, the phosphorus profile, $P(x, t)$, and the precipitate radius, $r(x, t)$ are modeled along the wafer thickness, x, as a function of processing time, t, using a finite element mesh.

The formation of the typical kink and tail-profile of the P emitter is described by a semi-empirical model developed by Bentzen *et al.* [9]. The P diffusion is described by Fick's law

$$\frac{\partial[P]}{\partial t} = \frac{\partial}{\partial x}\left(D_P([P])\frac{\partial[P]}{\partial x}\right) \tag{1}$$

where the diffusion of P atoms takes place via two different mechanisms: (1) via Si vacancies, V, and (2) via Si self-interstitials, I. The P diffusivity also is assumed to depend on the local P concentration, [P(x)], so that $D_P = D_{P,I} + D_{P,V} = D_P[P]$. Both diffusivities depend exponentially on the temperature, T.

To describe the kinetics of iron atoms within the silicon, we used the diffusion segregation equation, which was introduced by Tan *et al.* [10]:

$$\frac{\partial C_i}{\partial t} = \frac{\partial}{\partial x}\left[D_{Fe}\left(\frac{\partial C_i}{\partial x} - \frac{C_i}{\sigma}\frac{\partial \sigma}{\partial x}\right)\right] \tag{2}$$

The first term on the right represents Fick's law of diffusion, with D_{Fe}, the temperature-dependent diffusion coefficient of iron in Si, while the second term on the right allows the introduction of a space-dependent segregation coefficient, $\sigma(x)$.

The space-dependent segregation coefficient of iron in the phosphorus layer has been modeled by applying a semi-empirical model developed by Haarahiltunen *et al.* [11]:

$$\sigma(x) = 1 + V_{Si}K_{eq,1}\frac{n(x)}{n_i}(1 + K_{eq,2}[P(x)]) \tag{3}$$

Here, V_{Si} is the concentration of Si vacancies and $K_{eq,1}$ and $K_{eq,2}$ are equilibrium constants characterizing the reactions between Fe interstitials, Si vacancies, and P dopant atoms. The concentration of positively charged P atoms, $[P(x)]$, and the electron concentration, $n(x)$, depends on the space variable, x, and determine the dependence of σ on x.

To account for the dissolution of precipitated iron atoms, we apply Ham's law [12]:

$$\frac{\partial C_i}{\partial t} = 4\pi N r D_{Fe}(C_{eq,Fe} - C_i). \tag{4}$$

Here, $C_{eq,Fe}$ is the temperature-dependent solid solubility of iron in Si. We assume that all precipitated iron, $C_{p,0}$, is present in form of stoichiometric, low-temperature beta iron silicide, β-$FeSi_2$, [13] with a precipitate density N. The

variation of the precipitate radius, r, is described as

$$\frac{\partial r}{\partial t} = V_{Fe} D_{Fe} \frac{(C_i - C_{eq,Fe})}{r}, \tag{5}$$

where V_{Fe} is the volume of the primitive cell in β-$FeSi_2$ that contains one Fe atom.

Generally, the total content of a certain metal impurity within the material can be easily determined by bulk analysis, but its distribution, i.e., the mean precipitate density and radius, are unknown parameters and can strongly vary for different Si materials [14]. In this work, we use the as-grown precipitate density and initial radius as fit parameters. We assume that the initially precipitated iron $C_{p,0}$ is distributed with a precipitate density, N, and with a mean radius of r_0. The relation between both parameters is determined through the volume of the primitive cell in β-$FeSi_2$ [13]:

$$N = \frac{C_{p,0} V_{Fe}}{\frac{4}{3}\pi r_0^3} \tag{6}$$

To reduce the number of fit parameters over the ingot height in Section 3.2.1, two extreme cases are simulated where either N or r_0 is assumed to remain constant. In reality, both parameters can vary over the ingot height and also throughout the Si wafer, mainly depending on the density of heterogeneous nucleation sites.

Our model does not take into account the formation of new iron precipitates, i.e., precipitate nucleation. However, the dissolved interstitial iron, Fe_i, is the most detrimental chemical state of iron in Si. As the kinetic model can accurately estimate the flow of Fe_i from precipitates into the bulk, and from the bulk into the highly P-doped surface region, in a first approximation the formation of new precipitates can be ignored for cell processing. Furthermore, according to classical nucleation theory [15], the density of precipitates is limited to the number of existing nucleation sites. Due to a high energy barrier to homogeneous nucleation in Si, iron nucleates heterogeneously, limiting the possible nucleation sites for iron to crystalline defects such as dislocations, grain boundaries, or other precipitates. Therefore, the number of newly forming iron precipitates during standard solar cell processing is assumed to be negligible when precipitate densities up to 10^8 cm^{-3} already exist in the as-grown wafer [14]. However, nucleation cannot be ignored during crystal growth, and any model of impurity distribution during growth must account for nucleation kinetics.

2.2. Translation of the final iron distribution into charge carrier lifetime

Once the final iron distribution resulting from thermal processing has been calculated, it is translated into a distribution of electron and hole lifetime throughout the wafer thickness. Charge carrier recombination at interstitial iron atoms or at iron-boron (Fe-B) pairs is described by Shockley-Read-Hall statistics under low injection conditions [16,17]:

$$\frac{1}{\tau_i} = C_i \sigma v_{th} \tag{7}$$

Here, σ is the minority carrier capture cross-section (CCS), v_{th} is the thermal velocity of minority carriers, and τ_i is the calculated minority carrier lifetime limited by interstitial iron or Fe-B pairs.

Recombination at iron silicide precipitates is described by the following expression [18]:

$$\frac{1}{\tau_p} = 4\pi r^2 N \frac{sD/r}{s + D/r} \tag{8}$$

Here, τ_p is the precipitate-limited lifetime, while r and N are the mean precipitate radius and density, respectively, D is the minority carrier diffusion length in Si, and $s = 5 \cdot 10^6$ cm/s is the carrier recombination velocity at the precipitate surface [**?**].

2.3. Solar cell performance as a function of lifetime distribution

Within *PC1D*, the device can be divided into regions of different lifetimes corresponding to the lifetime distribution after solar cell processing. For example, the lifetime regions can be made to correspond to the near-surface highly-doped phosphorus layer, the depletion region, and the bulk. The P profile resulting from the diffusion-gettering simulation is imported as an external emitter profile in *PC1D*.

3. MODEL VALIDATION

To validate our model, we first consider the simulation of reported experimental results of gettering in highly-contaminated sc-Si and then proceed to compare our model against experimental data for gettering in mc-Si. Finally, the results on both material types are compared.

3.1. Single-crystalline silicon: diffusion and gettering

Shabani *et al.* [20] performed gettering experiments on intentionally contaminated Czochralski-grown wafers (CZ-Si). They applied Inductively Coupled Plasma Mass Spectroscopy (ICP-MS) to determine the total Fe concentration before and after PDG at different process temperatures and for different gettering times. Furthermore, they determined the surface concentration profiles of phosphorus and of different metal impurities after a 90 min PDG at 900°C by means of Secondary Ion Mass Spectroscopy (SIMS).

Introducing Shabani *et al.*'s time–temperature profiles and measured bulk iron concentrations into the I2E simulator, we modeled the thermal diffusion and calculated the resulting iron and phosphorous concentration profiles

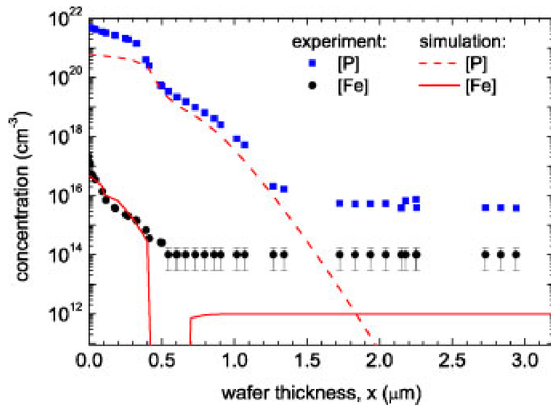

Figure 2. SIMS profiles of [P] (squares) and [Fe] (circles) after 90 min PDG at 900°C measured by Shabani *et al.* [20]; simulated curves shown as lines; measured [Fe] values for $x \geq 0.5$ μm correspond to the detection limit of SIMS; similarly, measured [P] values for $x \geq 1.5$ μm appear to reflect the detection limit for P in Si for the experimental setup.

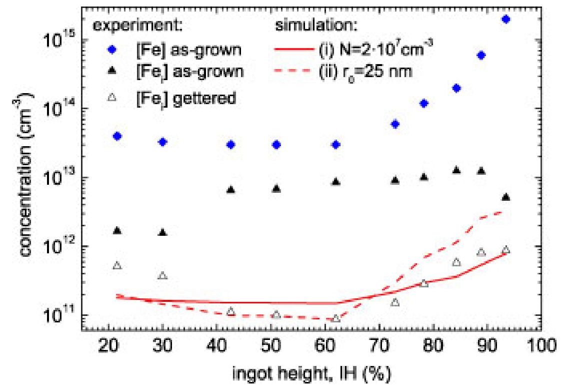

Figure 3. Total and dissolved iron concentrations over the ingot height measured on as-grown wafers (full diamonds and triangles) and [Fe$_i$] on P-diffused wafers (open triangles) [24,25] (total [Fe] are interpolated experimental values); calculated [Fe$_i$] for two different as-grown conditions: (i) a constant as-grown precipitate density of $N = 10^7$ cm^{-3} (solid line) and (ii) a constant as-grown precipitate radius of $r_0 = 25$ nm (dashed line).

after gettering versus depth from the wafer surface, x. Results are shown in Figure 2. The P concentration profile was simulated by applying Bentzen *et al.*'s P diffusion model, (Equation (1)). The concentration, P_0, at the wafer surface was chosen as a fit parameter. For any P_0, the model results in a poor fit of the data in the near-surface high-concentration region due to the formation of P clusters that are not accounted for in the model. Nevertheless, choosing $P_0 = 6 \cdot 10^{20}$ cm^{-3}, the tail of the P profile fits fairly well. This value is slightly higher than the P solid solubility limit in Si of about [P] = $5.3 \cdot 10^{20}$ cm^{-3} at 900°C [21].

The efficiency of PDG strongly depends on the as-grown distribution of the precipitated metal atoms [22], i.e., on the density and size of precipitates. Both parameters are unknown in Shabani *et al.*'s experiment so that the as-grown precipitate radius r_0, which is assumed to be constant throughout the Si wafer, has also been chosen as a fit parameter as described in Reference [23].

The simulated Fe profile fits the experimental profile quite well for $x \leq 0.4$ μm. For higher x, the measured SIMS profile reflects the detection limit of Fe, whereas the simulated curve reflects the final bulk concentration of [Fe] = $1.5 \cdot 10^{12}$ cm^{-3}, as measured by ICP-MS [20]. For $0.4 \leq x \leq 0.7$ μm, the simulation results in a narrow region completely depleted of iron. Due to the finite x-grid, [Fe$_i$] drops from $2 \cdot 10^{14}$ cm^{-3} at $x = 0.4$ μm to 0 cm^{-3} at $x = 0.5$ μm. In the semi-logarithmic presentation, this leads to the abrupt drop of the simulated Fe profile in this region between the high-concentration P layer and the p-type bulk.

3.2. Multi-crystalline silicon

3.2.1. Diffusion and gettering.

In the framework of the European Integrated Project *Crystal Clear*, mc-Si ingots were grown from very pure Si that was intentionally contaminated with 53 ppmw of iron [24]. The total and the dissolved iron concentrations, [Fe] and [Fe$_i$], were measured at different heights along the p-type ingot on as-grown wafers ([Fe$_i$] correspond to the mean value of C_i in Equations (1)–(7) over the wafer thickness). Additionally, [Fe$_i$] was measured on P-diffused samples [25].

We calculated the post-diffusion [Fe$_i$] along the ingot height (IH), taking the measured [Fe] and [Fe$_i$] as input parameters for the I2E simulator. As initial condition of the simulation, we specify either a constant as-grown radius for all heights such that r_0 = constant and $N = N(IH)$, or alternatively a constant as-grown precipitate density where N = constant and $r_0 = r_0(IH)$. The measured and calculated values are shown in Figure 3. A time–temperature profile close to the standard industrial P diffusion process was assumed. The rapid thermal annealing step applied for contact firing has not been simulated as the experimental results show that it has a relatively low impact on the iron distribution [25]. Based on typical values of mean radius and precipitate density in mc-Si [14], two different iron distributions were considered. In the first simulation, (i), the precipitate density was assumed to be constant over the ingot height with a value of $N = 2 \cdot 10^7$ cm^{-3}. This leads to an increase of the as-grown precipitate radius from about 25 nm at the center of the ingot to 97 nm towards the top. In the second simulation, (ii), a constant as-grown precipitate radius of $r_0 = 25$ nm was chosen, leading to a variation of the precipitate density from about $N = 10^7$ to 10^9 cm^{-3} over the ingot height.

The constant-as-grown-radius simulation (ii) (dashed line) results in a very good fit of the measured [Fe$_i$] in the center of the ingot, but the calculated values are much higher than the measured ones towards the top of the ingot. In contrast, in the constant-density simulation (i) (solid line), we achieve a fairly good fit of the measured [Fe$_i$] at the top and at the center of the ingot. With increasing iron content

towards the top of the ingot, our simulations suggest that iron silicide precipitates mainly increase in size, with spatial density increasing only slightly, from about $1 \cdot 10^7$ cm^{-3} to $2 \cdot 10^7$ cm^{-3}.

At the bottom of the ingot, in both cases the calculated [Fe_i] after PDG is lower than the measured values. In general, the density of both structural defects and oxygen precipitates has been observed to increase towards the ingot bottom, providing many favorable nucleation sites for metal precipitates. In this case, the mc-Si ingot in consideration is a laboratory-scale ingot of only 110 mm height, such that the defective bottom region extends much further into the center of the ingot than for commercially available mc-Si ingots.

The higher concentration of defects other than Fe in this deteriorated bottom region might be responsible for the poor gettering response observed there. Using our simulation tool to study this potential degradation effect, we find that for a given total [Fe], a higher density of smaller precipitates leads to faster dissolution during high-temperature steps, increasing [Fe_i] locally. Given experimental evidence that areas of high dislocation density respond poorly to PDG with low minority carrier lifetimes remaining after processing [26,27], we suspect that the locally elevated interstitial iron population at the bottom of the ingot is trapped in the bulk by defect interactions.

The effect of defects other than Fe has not been taken into account in the I2E simulation, where a homogeneous distribution of β-$FeSi_2$ precipitates in each wafer was assumed. The actual distribution of iron precipitates along the height of the ingot has been studied by means of micro- X-Ray Fluorescence and will be discussed and compared to the simulation results in a separate publication [28].

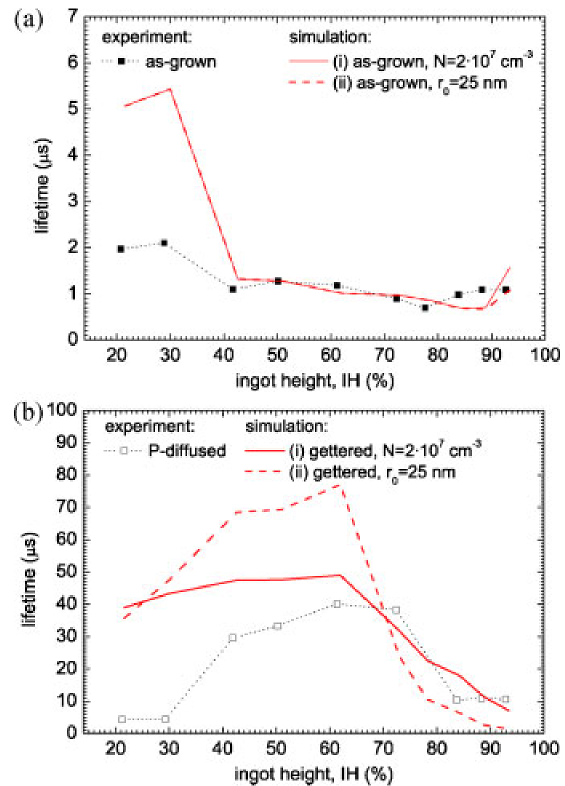

Figure 4. Electron lifetimes measured on (a) as-grown (full squares) and (b) P-diffused wafers (open squares) as a function of the ingot height in intentionally Fe-contaminated cast mc-Si [25]; simulated electron lifetimes for (a) as-grown Fe distributions and (b) Fe distributions after PDG; constant-density simulations (i) as solid lines, constant-radius simulations (ii) as dashed lines.

.

3.2.2. Charge carrier lifetime.

For further model validation, the electron lifetime in as-grown and P-diffused samples was calculated along the height of the intentionally Fe-contaminated mc-Si ingot of Section 3.2.1. The electron lifetime is determined by recombination at dissolved and precipitated iron as described in Equations (7) and (8). We calculated the resulting electron lifetime for the two as-grown iron distributions assumed in simulations (i) and (ii) and for the resulting iron distributions after PDG simulation. It was assumed that all dissolved iron is present in form of Fe-B pairs (lifetime measurement conditions). The corresponding electron CCS, $\sigma_e^{Fe-B} = 5 \cdot 10^{-15}$ cm^2, was taken from Reference [29]. No other lifetime-limiting defects apart from Fe-B pairs and β-$FeSi_2$ precipitates were taken into account. In Figure 4(a) and (b), the calculated lifetime distributions for as-grown and gettered wafers are plotted as a function of ingot height. The actual effective lifetime values measured by means of Quasi-Steady State Photoconductance on SiN_x passivated, as-grown ((a) full squares) and P-diffused samples ((b) open squares) as reported in Reference [25] are also shown. The measured values are given for an injection level of $\Delta n = 10^{15}$ cm^{-3} while the simulations were done under the assumption of low injection conditions. A potential discrepancy is assumed to be negligible given that the Fe-B pair dominated electron lifetime measured on mc-Si wafers is usually nearly independent of the injection level in this range [30].

The as-grown lifetime in the middle and at the top of the ingot is dominated by dissolved iron, which is present in concentrations above 10^{13} cm^{-3} and leads to electron lifetime below 1 µs. Thus, the distribution of precipitated iron has little influence on the lifetime throughout the ingot. This results in similar calculated as-grown lifetime values for simulations (i) and (ii).

The measured lifetime at the bottom of the ingot is much lower than the calculated values both before and after gettering. This is attributed to a higher density of oxygen precipitates and crystal defects, which e.g., Coletti *et al.* [25] suggested dominate the minority carrier lifetime at the bottom of the ingot and are not affected by external gettering.

For the middle and top of the ingot, after PDG the concentration of dissolved iron is drastically reduced and the charge carrier lifetime then strongly depends on the distribution of the precipitated iron, as can be observed in the

simulated lifetime curves for gettered wafers in Figure 4. The calculated lifetime values are much closer to the measured ones when a constant precipitate density over the ingot height is assumed, as in simulation (i). This result indicates that there appears to be only a weak variation of precipitate density along the ingot height.

The measured lifetime values are about 10 to 40 μs lower than the simulated lifetimes up to about 70% ingot height. Lifetime values measured by QSSPC are effective lifetimes and might be lower than the Fe-related bulk lifetime due to non-zero surface recombination velocity (SRV) and due to other lifetime-limiting defects. The latter might be structural defects and other impurity atoms apart from Fe which are not taken into account in the simulations. Iron-related defects seem to pre-dominate the electron lifetime for ingot heights > 70%.

3.2.3. From impurity distribution to solar cell efficiency.

To validate the I2E model as a whole, solar cell efficiencies along the height of the intentionally contaminated p-type mc-Si ingot were simulated with *PC1D*. As input parameters, we used the P emitter profile calculated in Section 3.2.1 and further cell parameters shown in Table I. The final charge carrier lifetimes were re-calculated using the minority carrier CCS of interstitial iron in Equation (7), assuming that at one sun illumination all Fe-B pairs are dissociated (solar cell operation conditions).

The published values of the electron CCS of Fe_i in p-Si differ by one order of magnitude [31–33]. The different CCS values have a significant influence on the absolute value of the calculated lifetime and ultimately the solar cell efficiency, but the overall trends along the ingot height remain relatively unchanged with different Fe_i CCS. For the present simulations, we have chosen the latest reported value, $\sigma_e^{Fe_i} = 1.3 \cdot 10^{-14}\,\text{cm}^2$, published by Macdonald *et al.* [33].

The simulated efficiency values are compared to measured efficiencies published in Reference [34] and are shown in Figure 5(a). The measured efficiencies along the reference ingot are also shown. Between 50 and 80% ingot height, both calculated efficiency curves fit the measured values very well although the simulated lifetimes in this range differ strongly among each other and also from the measured lifetimes (see Figure 4(a) and (b)). Furthermore, solar cell efficiencies of the contaminated ingot are nearly

Table I. Device parameters used for PC1D simulation of Coletti *et al.*'s solar cells; front SRVs (a) and (b) correspond to values chosen for simulations shown in Figure 5(a) and (b), respectively.

Parameter	Value
Wafer thickness (μm)	240
Device area (cm^2)	138
Base doping (cm^{-3})	$1.3 \cdot 10^{16}$
Front SRV (a) (cm/s)	$2 \cdot 10^6$
Front SRV (b) (cm/s)	$1 \cdot 10^6$
Back SRV (cm/s)	750

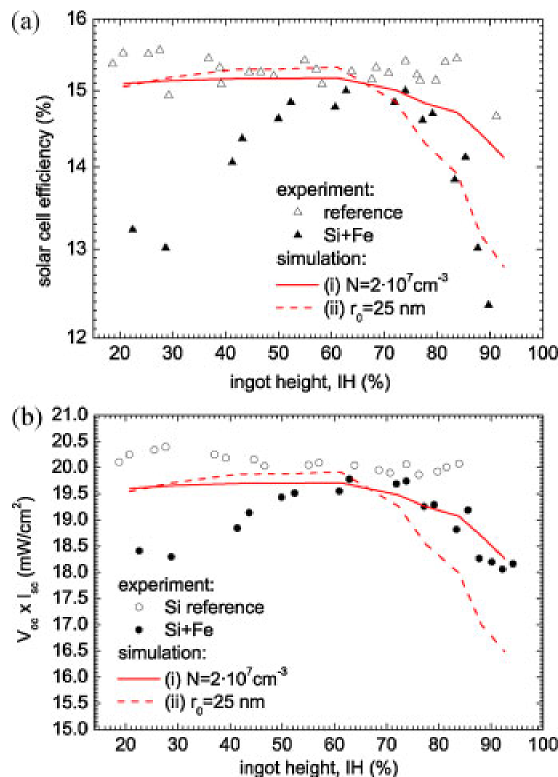

Figure 5. Solar cell performance as a function of the ingot height in intentionally-contaminated mc-Si and in the reference ingot [25]: (a) solar cell efficiency and (b) product of the open circuit voltage times the short circuit current; experimental data points as dots, simulated curves for as-grown iron distributions (i) and (ii) as lines.

as high as efficiencies of the reference ingot in this range. Thus, the electron lifetime does not seem to be the performance limiting factor in the center range of the ingot.

As expected from the poor fit of the [Fe_i] and lifetime distribution at the bottom of the ingot (see Figures 3 and 4), the calculated solar cell efficiencies deviate significantly from the measured values below 50% ingot height. As mentioned before, this low device performance in the bottom region is most likely due to defects other than iron.

Further comparison of Figures 4(b) and 5(a) show that the decrease in modeled lifetime towards the top of the ingot results in a degradation of the simulated solar cell efficiency. However, for ingot heights > 80%, the measured efficiency degradation is more pronounced and cannot be explained by the decreasing bulk lifetime alone, especially for the constant-as-grown-density simulation (i). The additional efficiency degradation is probably due to the drop in the fill factor that has been measured from about 80% ingot height upwards [25].

This drop in the fill factor at the top of the ingot may be due to shunts that arise from either silicon-carbide and silicon-nitride microdefects, metal precipitates, or both. The carbon concentration increases towards the top of the ingot, and SiC microdefects have been shown to lead to important

shunt losses [35]. Iron precipitates have been recently observed at voltage pre-breakdown sites in mc-Si solar cells as well [36]. Additionally, dendritic crystal growth has been observed for very high iron concentrations towards the ingot top [24], which might favor the formation of such second-phase particles.

To remove the influence of varying fill factors on solar cell performance, we simulated the product of open circuit voltage and short circuit current, $V_{oc} \times I_{sc}$, along the ingot height. The front SRV had to be adjusted to a lower value of $1 \cdot 10^6$ cm/s so that a $V_{oc} \times I_{sc}$ value of about 20 mW/cm^2 resulted for a measured bulk lifetime of about 80 μs along the reference ingot. In Figure 5(b), the simulated curves as well as the experimental values measured on the reference p-type ingot and the Fe-contaminated p-type ingot [25] are plotted.

The simulated curve for the constant-as-grown-density distribution (i) gives a reasonable fit to the experimental data, except for the bottom of the ingot. The constant-as-grown-radius simulation (ii) slightly underestimates the actual $V_{oc} \times I_{sc}$ values at the top of the ingot where the simulated lifetimes are also lower than the measured ones (see Figure 4(b)). Nevertheless, the data largely fall between the constant-as-grown-radius and constant-density simulations suggesting that both parameters, the precipitate density, and radius, increase with increasing [Fe] along the ingot height. Actually, we observe a variation of both parameters in our preliminary experimental results, which will be published shortly [28].

The reasonable modeling of $V_{oc} \times I_{sc}$ at the top of the ingot leads to an important conclusion: besides the charge carrier lifetime, fill factor losses are potentially an equally dominant performance-limiting factor in highly metal-contaminated materials. These fill factor losses are presumably due to shunting caused by metal precipitates incompletely dissolved by P-diffusion gettering and remaining in the space-charge region.

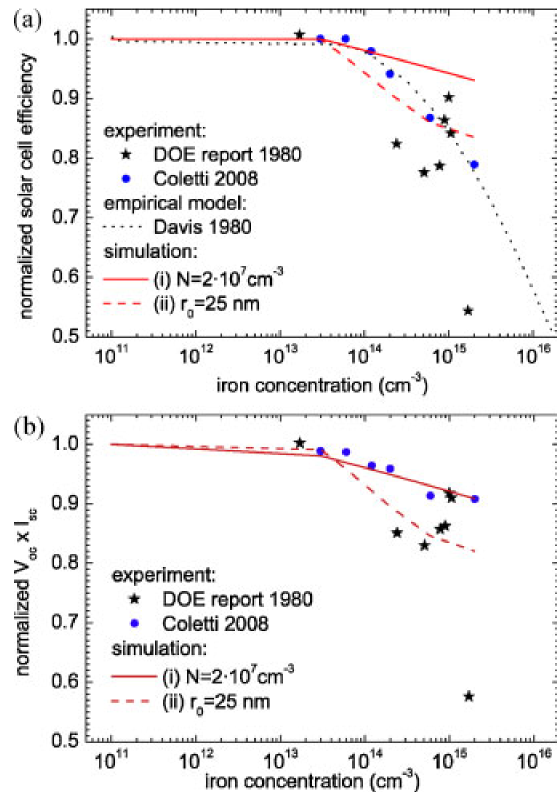

Figure 6. Solar cell performance as a function of the total iron content measured in intentionally-contaminated CZ-Si wafers (stars) from Reference [39] and the fit of the data based on an empirical model published by Davis *et al.* [37] (dotted line); corresponding data measured along an intentionally contaminated p-type cast mc-Si ingot (circles) and our simulated solar cell performance along the same mc-Si ingot [25] assuming lifetime degradation only (solid and dashed lines); (a) solar cell efficiency; (b) open circuit voltage times short circuit current.

3.3. Single-crystalline versus multi-crystalline silicon: I2E simulations

The solar cell efficiencies obtained on intentionally Fe-contaminated mc-Si ingots are compared to results of the famous Westinghouse study from the early 1980s. In the Westinghouse study, solar cell efficiencies were determined as a function of the total metal content in CZ-Si ingots that were intentionally contaminated with different metal types, one of them iron. The results were published in Reference [37–39]. In Figure 6(a), the normalized experimental solar cell efficiencies as well as a fit of these values based on an empirical model published by Davis *et al.* [37] are shown. Furthermore, normalized experimental efficiency values as a function of total iron content along the mc-Si ingot height from Coletti *et al.* are plotted. Coletti *et al.*'s and Davis *et al.*'s data sets were independently normalized to their respective maximum efficiency of samples with low Fe concentration.

The solid line in Figure 6(a) shows the simulated solar cell efficiency that we would expect if the device were limited only by bulk charge carrier recombination at interstitial iron and iron silicide precipitates. The simulated curve results in a good fit of the experimental values for total as-grown iron concentrations $\leq 10^{14}$ cm^{-3}. Iron at these levels is expected to be the dominant lifetime-limiting defect in cells coming from the center of ingots grown from heavily contaminated feedstock materials such as SoG-Si and in any cells from the red-zone border region throughout much of the height of industrial ingots of any feedstock quality.

Because of the large scattering of Davis *et al.*'s data for high [Fe], it seems unlikely that there is efficiency reduction due to systematic decrease in electron lifetime. The scatter in Davis *et al.*'s data may also be due to experimental imprecision, as Fe content was typically measured in only one wafer, while cell results were averaged over entire ingots [39].

Surprisingly, the experimental values published in 2008 for mc-Si follow the fitted curve from Davis *et al.* quite

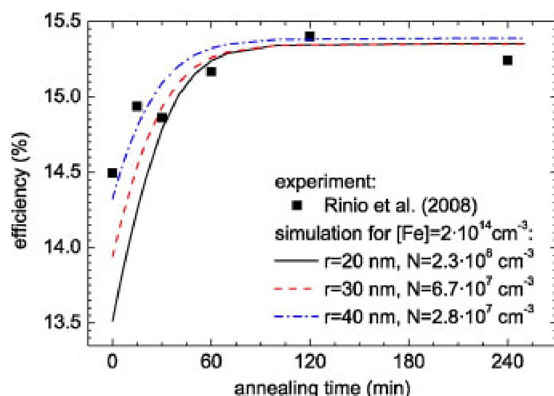

Figure 7. Solar cell efficiencies on p-type mc-Si ingot border wafers; the 10 min P emitter diffusion at 900°C was followed by a LTA at 500°C during different annealing times.

exactly. This is an unexpected result, as the two studies involved, applied very different process technologies to very different Si materials.

Again, to remove the influence of the fill factor on solar cell performance, the normalized product of open circuit voltage and short circuit current, $V_{oc} \times I_{sc}$, taken from the DOE report [39] has been plotted as a function of [Fe] in Figure 6(b). As before, the resulting data points, after removing the fill factor losses, are much closer to our simulated curve (i) for constant-as-grown density distribution. This result suggests again that for total iron concentrations $>10^{14}$ cm^{-3}, device shunting due to large metal precipitates may be an equally significant cause of performance loss as lifetime degradation, independent of the material type and processing.

4. TOWARDS PROCESS OPTIMIZATION

Besides the simulation of standard solar cell processes on different material types, the I2E simulation tool can be employed to understand very recent experiments on solar cell process optimization and to guide further experiments in alternative processing. To this end, we show simulated results of an experiment on low temperature annealing (LTA) that was recently carried out by Rinio *et al.* [40]. Solar cells were made out of wafers from the border of a p-type mc-Si ingot where iron is presumed to be the principle lifetime-limiting impurity. After P emitter diffusion at 900°C for 10 min, the wafers were subjected to an LTA at 500°C for different times ranging from 15 min up to 4 h. In Figure 7, the experimental values as well as the simulated solar cell efficiencies for different as-grown iron distributions as a function of annealing time are shown. As the total as-grown iron content as well as the distribution of iron are unknown, a total concentration of $2 \cdot 10^{14}$ cm^{-3} has been assumed and the as-grown precipitate radius, r_0, has been varied. Lateral inhomogeneities of the Fe distribution due to in-diffusion from the crucible walls have not been taken into account

Table II. Device parameters used for PC1D simulation of Rinio *et al.*'s solar cells.

Wafer thickness (μm)	240
Device area (cm^2)	138
Base doping (cm^{-3})	$1 \cdot 10^{16}$
Front SRV (cm/s)	$4 \cdot 10^{6}$
Back SRV (cm/s)	1300

in the simulation. Further solar cell parameters that are not given in the literature have been chosen such that the experimental points are well-fit and are shown in Table II.

Too many input parameters are unknown to perform truly quantitative simulations. Nevertheless, an important trend in the efficiency improvement due to LTA can be observed: independent of the as-grown precipitate radius, more than 90% of the efficiency increase occurs during the first 60 min of LTA at 500°C. According to our model calculations, this increase is due to the reduction of interstitial iron in the bulk, much of it having been gettered to the P-rich layer, in agreement with experimental results [41,42]. With decreasing temperature, the Fe precipitation and segregation to the P rich layer increases while precipitate dissolution becomes insignificant. For longer annealing times, a further efficiency increase is inhibited by recombination at iron silicide precipitates.

5. DISCUSSION

From the good agreement between existing experimental data and our simulation results, we conclude that the I2E model captures the two most important kinetic phenomena for solar cell processing of Fe-contaminated wafers: iron precipitate dissolution and iron interstitial gettering. These two phenomena appear to play a dominant role in determining minority carrier lifetime in mc-Si (and by extension, cell performance), since Fe_i is a principal lifetime-limiting defect in the middle, top, and edges of standard mc-Si ingots. Modeling confirms that the distribution of iron, not only its total concentration, is crucial in determining the material's response to high-temperature treatments [4,5].

The observation that the [Fe_i] profile along the ingot height after PDG follows the profile of the total [Fe] in as-grown samples [25] is well-explained by our model. The removal of iron by means of external gettering is mainly limited by two mechanisms: (1) the dissolution of iron precipitates and (2) the diffusion of dissolved iron towards the P-diffused surface. The constant dissolution of metal precipitates tends to increase [Fe_i] up to the solid solubility limit at the given process temperature, while the diffusion to the wafer surface tends to decrease [Fe_i] in the wafer bulk. Thus, during PDG, a quasi steady-state concentration of dissolved iron below its solid solubility is established. As an example, the evolution of the bulk Fe_i concentration during a 20 min PDG at 850°C is shown as a function of total as-grown iron concentration in Figure 8. Iron segregation to the near-surface P layer decreases [Fe_i] below the

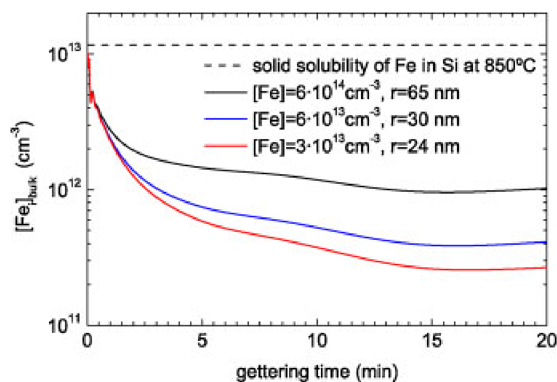

Figure 8. Evolution of the mean [Fe_i] in the wafer bulk during PDG as a function of total [Fe] for a constant precipitate density of $N = 2{\cdot}10^7$ cm^{-3}.

solid solubility limit of about 10^{13} cm^{-3} at 850°C. A quasi steady-state concentration is established within 15 min. As the dissolution kinetics of metal precipitates strongly depend on their size and density (Equation (4)), the final value of [Fe_i] also depends on the precipitate distribution. In Section 3.2.1, we show that we expect the precipitate size to increase markedly with increasing [Fe] along the ingot height. The smaller precipitates in the center of the ingot are likely to completely dissolve during PDG and only a low concentration of dissolved iron remains. With increasing precipitate size but largely constant precipitate density towards the top of the ingot, more iron dissolves into the wafer bulk during high-temperature processing due to an increasing interface area between iron precipitates and the silicon matrix. The large, dissolving iron precipitates act as efficient sources of Fe interstitials and lead to an increase of the measured [Fe_i] towards the top of the ingot.

Other iron-related kinetics not currently captured by the I2E model, including Ostwald ripening and internal gettering, appear to play a minor role in dictating the [Fe_i] distribution during standard mc-Si solar cell processing. Experiments have shown that external gettering dominates over internal effects for iron when a P-diffused layer is present [41,42].

To extend the predictive capability of the model, it is desirable to investigate and model the lifetime-limiting defect interactions that occur at the bottom of typical mc-Si ingots. A high oxygen concentration and dislocation density in particular are suspected to be major causes of the lifetime degradation and poor gettering response at the bottom of the ingot.

6. CONCLUSIONS

The I2E simulator we have developed allows one to calculate final solar cell performance as a function of the as-grown iron content and distribution in the Si wafer, the time–temperature profiles during solar cell processing, and the device architecture. We have successfully validated the three standalone parts of our model, comparing our simulations to experimental results published on sc-Si and mc-Si materials.

The I2E model results provide insight into the different mechanisms that dominate the effectiveness of PDG and the final solar cell performance in highly Fe-contaminated material. With increasing iron content along a mc-Si ingot, both iron distribution-related parameters, the precipitate size and density seem to vary. Poor device performance associated with wafers from the top of the ingot appears to be strongly influenced by decreases in fill factor, possibly related to shunting, besides the decreased minority carrier lifetime. This seems to be true for total iron concentrations above 10^{14} cm^{-3} in sc-Si and mc-Si wafers, and for different standard processing conditions.

For novel processing concepts, the I2E simulator can guide towards optimization of time–temperature profiles when a trade-off between efficiency increase and short process time has to be found for highly Fe-contaminated materials. For example, independent of the as-grown iron distribution, relative short annealing times at low temperatures after PDG appear to lead to an appreciable increase in solar cell efficiency.

ACKNOWLEDGMENTS

This work has been partially funded by the Spanish Ministerio de Ciencia e Innovación through Thincells project (TEC2008-06798-C03-02), by the U.S. Department of Energy, under contract number DE-FG36-09GO19001, and through the generous support of Doug Spreng and the Chesonis Family Foundation. D. P. Fenning acknowledges the support of the NSF Graduate Research Fellowship. The additional support through the MIT-Spain/La Cambra de Barcelona Seed Fund is gratefully acknowledged.

REFERENCES

1. Carnel L, Nyhus J, Helland K, Influence of wafer quality on cell performance, PV International 7.
2. Coletti G, Bronsveld P, Knopf C, Swanson C, Kvande R, Arnberg L, Habenicht H, Warta W, Impact of iron, nickel and chromium in feedstock on multicrystalline silicon solar cell properties, in: *Proc. 24th EUPVSEC*, Hamburg, Germany, 2009, pp. 1011–1014.
3. Hofstetter J, Lelièvre JF, del Cañizo C, Luque A, Acceptable contamination levels in solar grade silicon: From feedstock to solar cell, *Materials Science and Engineering: B* 2009; **159–160**: 299–304.
4. Plekhanov P, Gafiteanu R, Gösele U, Tan T, Modeling of gettering of precipitated impurities from si for carrier lifetime improvement in solar cell applications, *J. Appl. Phys.* 1999; **86**: 2453–2458.
5. Haarahiltunen A, Savin H, Yli-Koski M, Talvitie H, Asghar M, Sinkkonen J, As-grown iron precipitatesand get-

tering in multicrystalline silicon, *Materials Science and Engineering B* 2008; **159–160**: 248–252.
6. Sopori BL, Jastrzebski L, Tan T, A comparison of gettering in single-and multicrystalline silicon for solar cells, in: *25th IEEE PV Specialists Conference*, 1996; p. 625.
7. Naerland TU, Arnberg L, Holt A, Origin of the low carrier lifetime edge zone in multicrystalline pv silicon, *Prog. Photovoltaics res. appl.* 2008; **17**: 289–296.
8. Basore P, Clugston DA, Pc1d version 4 for windows: from analysis to design, Proceedings of the 25th IEEE Photovoltaic Specialists Conference 1996; 377–381.
9. Bentzen A, Holt A, Christensen JS, Svensson BG, High concentration in-diffusion of phosphorous in si from a spray-on source, *Journal of applied physics* 2006; **99**: 064502.
10. Tan TY, Gafiteanu R, Joshi SM, Gösele U, Semiconductor Silicon, Electrochemical Society, 1998, Ch. 6, p. 1050.
11. Haarahiltunen A, Savin H, Yli-Koski M, Talvitie H, Sinkkonen J, Modeling phosphorous diffusion gettering of iron in single crystal silicon, *Journal of applied physics* 2009; **105**: 023510.
12. Ham F, Theory of diffusion limited precipitation, *J. Phys. Chem. Solids 6* 1958; 335.
13. Dusausoy Y, Protas J, Wandji R, Roques B, Structure cristalline du disiliciure de fer, *fesi$_2$, Acta Cryst. B27* 1971; 1209.
14. Buonassisi T, Istratov A, Marcus M, Lai B, Cai Z, Heald S, Weber E, Engineering metal-impurity nanodefects for low-cost solar cells, *Nat. Mater.* 2005; **4**: 676–679.
15. Balluffi RW, Allen SM, Carter WC, Kinetics of materials, John Wiley and Sons, 2005.
16. Shockley W, Read JWT, Statistics of the recombinations of holes and electrons, *Phys. Rev.* 1952; **87**: 835–842.
17. Hall RN, Electron-hole recombination in germanium, *Phys. Rev.* 1952; **87**: 387.
18. del Cañizo C, Luque A, A comprehensive model for the gettering of lifetime-killing impurities in silicon, *J. Electrochem. Soc.* 2000; **147**: 2685–2692.
19. Plekhanov PS, Tan TY, Schottky effect model of electrical activity of metallic precipitates in silicon, *Appl. Phys. Lett.* 2000; **76**: 3777.
20. Shabani MB, Yamashita T, Morita E, Study of gettering mechanism in silicon: competitive gettering between phosphorous diffusion gettering and other gettering sites, *Solid state phenomena* 2008; **131–133**: 399–404.
21. Solmi S, Parisini A, Angelucci R, Armigliato A, Nobili D, Moro L, Dopant and carrier concentration in si in equilibrium with monoclinic sip precipitates, *Phys. Rev. B* 1996; **53**: 7836–7841.
22. Tan TY, Plekhanov P, Joshi SM, Gafiteanu R, Gösele U, Physics of impurity gettering in pv silicon, in: Proc. 8th workshop on crystalline silicon solar cell materials and processes, *Copper Mountain*, Colorado, USA, 1998, pp. 42–49.
23. Hofstetter J, Fenning DP, Lelièvre JF, Bertoni MI, Buonassisi T, del Cañizo C, Simulating the evolution of the iron content and distribution during solar cell processing, in: *Proc. 24th EUPVSEC*, Hamburg, Germany, 2009, pp. 2019–2022.
24. Kvande R, Geerligs B, Coletti G, Arnberg L, Sabatino MD, Ovrelid EJ, Swanson CC, Distribution of iron in multi-crystalline silicon ingots, *Journal of applied physics* 2008; **104**: 064905.
25. Coletti G, Kvande R, Mihailetchi VD, Geerligs LJ, Arnberg L, Øvrelid EJ, Effect of iron in silicon feedstock on p- and n-type multicrystalline silicon solar cells, *Journal of applied physics* 2008; **104**: 104913.
26. Kittler M, Seifert W, Estimation of the upper limit of the minority-carrier diffusion length in multicrystalline silicon: Limitation of the action of gettering and passivation on dislocations, *Solid State Phenomena* 2004; **95/96**: 197–204.
27. Bentzen A, Holt A, Kopecek R, Stokkan G, Christensen JS, Svensson BG, Gettering of transition metal impurities during phosphorus emitter diffusion in multicrystalline silicon solar cell processing, *J. Appl. Phys.* 2006; **99**: 093509.
28. Fenning DP, Hofstetter J, Bertoni MI, Lelièvre JF, Coletti G, del Cañizo C, Buonassisi T, Synchrotron-based microanalysis and predictive modeling of iron distribution and solar cell efficiency along the height of a multicrystalline silicon ingot, in: *Proc. 35th IEEE PVSC*, Honolulu, Hawaii, 2010.
29. Macdonald D, Roth T, Deenapanray PNK, Trupke T, Bardos RA, Doping dependence of the carrier lifetime crossover point upon dissociation of iron-boron pairs in crystalline silicon, *Applied Physics Letters* 2006; **89**: 142107.
30. Macdonald DH, Geerligs LJ, Azzizi A, Iron detection in crystalline silicon by carrier lifetime measurements for arbitrary injection and doping, *J. Appl. Phys.* 2004; **95 (3)**: 1021–1028.
31. Istratov A, Hieslmair H, Weber ER, Iron and its complexes in silicon, *Appl. Phys. A* 1999; bf 69: 13–44.
32. Reina S, Glunz SW, Electronic properties of interstitial iron and iron-boron pairs determined by means of advanced lifetime spectroscopy, *Journal of Applied Physics* 2005; **98**: 113711.
33. Macdonald D, Tan J, Trupke T, Imaging interstitial iron concentrations in boron-doped crystalline silicon using photoluminescence, *Journal of Applied Physics* 2008; **103**: 073710.
34. Coletti G, Bronsveld P, Kvande R, Geerligs L, Arnberg L, Habenicht H, Warta W, Knopf C, Impact of transition metals in feedstock on multicrystalline silicon solar

cell properties, in: *Proc. 18th Photovoltaic Solar Energy Conference*, Kolkata, India, 2009.
35. Bauer J, Breitenstein O, Rakotoniaina J-P, Electronic activity of sic precipitates in multicrystalline solar silicon, *phys. stat. sol. (a)* 2007; **204**: 2190.
36. Kwapil W, Gundel P, Schubert MC, Heinz FD, Warta W, Weber ER, Goetzberger A, Martinez-Criado G, Observation of metal precipitates at prebreakdown sites in multicrystalline silicon solar cells, *Applied Physics Letters* 2009; **95**: 232113.
37. Davis JR, Rohatgi A, Hopkins RH, Blais PD, Rai-Choudhury T, McCormick JR, Mollenkopf HC, Impurities in silicon solar cells, *IEEE T. Electron. Dev.* 1980; **27**: 677–687.
38. Rohatgi A, Davis JR, Hopkins RH, Rai-Choudhury P, McMullin PG, McCormick JR, Effect of titanium, copper and iron on silicon solar cells, *Solid-State Electronics* 1980; **23**: 415–422.
39. Hopkins R, Davis JR, Rohatgi A, Campbell RB, Blais P, Rai-Choudhury P, Stapleton RE, Mollenkopf HC, McCormick JR, DOE report: Effect of Impuritiee and Processing on Silicon Solar Cells, Westinghouse R&D center, Pittsburgh, Pennsylvania, January 1980.
40. Rinio M, Yodyunyong A, Pirker M, Keipert S, Wang P, Buonassisi T, Borchert D, Defect redistribution by low temperature annealing in ingot silicon solar cells, in: *Proc. 23nd EUPVSEC*, Valencia, Spain, 2008, pp. 1014–1017.
41. Rinio M, Yodyunyong A, Pirker M, Zhang C, Günther D, Botchak P, Keipert S, Borchert D, Heuer M, Montesdeoca-Santana A, New results using a low temperature anneal in processing of multicrystalline solar cells, in: *Proc. 24th EUPVSEC* Hamburg, Germany, 2009, pp. 1816–1819.
42. Hofstetter J, Lelièvre JF, del Cañizo C, Luque A, Study of internal versus external gettering of iron during slow cooling processes for silicon solar cell fabrication, *Solid State Phenomena* 2010; **156–158**: 387–393.